Lesion Quantification Accuracy of Digital ^{90}Y PET Imaging in the Context of Dosimetry in Systemic Fibroblast Activation Protein Inhibitor Radionuclide Therapy

David Kersting[1,2], Walter Jentzen[1,2], Daniel Jeromin[1,2], Ilektra-Antonia Mavroeidi[2,3], Maurizio Conti[4], Florian Büther[5], Ken Herrmann[1,2], Christoph Rischpler[1,2], Rainer Hamacher[2,3], Wolfgang P. Fendler[1,2], Robert Seifert[1,2,5], and Pedro Fragoso Costa[1,2]

[1]Department of Nuclear Medicine, West German Cancer Center (WTZ), University Hospital Essen, University of Duisburg-Essen, Essen, Germany; [2]German Cancer Consortium (DKTK), Partner Site University Hospital Essen, Essen, Germany; [3]Department of Medical Oncology, West German Cancer Center (WTZ), University Hospital Essen, University of Duisburg-Essen, Essen, Germany; [4]Siemens Medical Solutions USA, Inc., Knoxville, Tennessee; and [5]Department of Nuclear Medicine, University Hospital Muenster, University of Muenster, Muenster, Germany

Therapy with ^{90}Y-labeled fibroblast activation protein inhibitors (^{90}Y-FAPIs) was recently introduced as a novel treatment concept for patients with solid tumors. Lesion and organ-at-risk dosimetry is part of assessing treatment efficacy and safety and requires reliable quantification of tissue uptake. As ^{90}Y quantification is limited by the low internal positron–electron pair conversion rate, the increased effective sensitivity of digital silicon photomultiplier-based PET/CT systems might increase quantification accuracy and, consequently, allow for dosimetry in ^{90}Y-FAPI therapy. The aim of this study was to explore the conditions for reliable lesion image quantification in ^{90}Y-FAPI radionuclide therapy using a digital PET/CT system. **Methods:** Two tumor phantoms were filled with ^{90}Y solution using different sphere activity concentrations and a constant signal-to-background ratio of 40. The minimum detectable activity concentration was determined, and its dependence on acquisition time (15 vs. 30 min per bed position) and smoothing levels (all-pass vs. 5-mm gaussian filter) was investigated. Quantification accuracy was evaluated at various activity concentrations to estimate the minimum quantifiable activity concentration using contour-based and oversized volume-of-interest–based quantification approaches. A ±20% deviation range between image-derived and true activity concentrations was regarded as acceptable. Tumor dosimetry for 3 patients treated with ^{90}Y-FAPI is presented to project the phantom results to clinical scenarios. **Results:** For a lesion size of 40 mm and a clinical acquisition time of 15 min, both minimum detectable and minimum quantifiable activity concentrations were 0.12 MBq/mL. For lesion sizes of greater than or equal to 30 mm, accurate quantification was feasible for detectable lesions. Only for the smallest 10-mm sphere, the minimum detectable and minimum quantifiable activity concentrations differ substantially (0.43 vs. 1.97 MBq/mL). No notable differences between the 2 quantification approaches were observed. For the investigated tumors, absorbed dose estimates with reliable accuracy were achievable. **Conclusion:** For lesion sizes and activity concentrations that are expected to be observed in patients treated with ^{90}Y-FAPI, quantification with reasonable accuracy is possible. Further dosimetry studies are needed to thoroughly investigate the efficacy and safety of ^{90}Y-FAPI therapy.

The high-energy β-particle emitter ^{90}Y is a radionuclide that is used in oncologic radionuclide therapy regimens. Typical applications include local radioembolization of hepatocellular carcinoma by selective internal radiation therapy (*1*) or systemic therapies using, for example, somatostatin receptor agonists like ^{90}Y-DOTATATE/DOTATOC to target neuroendocrine tumors after intravenous injection (*2*). Recently, systemic treatments of sarcoma or pancreatic cancer patients using ^{90}Y-labeled fibroblast activation protein (FAP) inhibitors (^{90}Y-FAPIs) were introduced (*3,4*). The target molecule, fibroblast activation protein α, is a cell surface dipeptidyl peptidase expressed by cancer-associated fibroblasts in the tumor microenvironment of various solid tumors as well as cancer cells such as sarcoma and mesothelioma (*5*).

Intratherapeutic ^{90}Y bremsstrahlung whole-body scintigraphy or SPECT imaging is established and well tolerated by patients for rapidly verifying tracer accumulation in the tumor tissue and for investigating tracer biodistribution (*6*). However, these imaging modalities do not allow reliable quantification of ^{90}Y activity concentrations, which is mandatory for intratherapeutic lesion dosimetry in systemic radionuclide therapy (*7*). Limiting factors are, for example, an inaccurate compensation of scattered and septal penetrating photons of the continuous bremsstrahlung energy spectrum and the difficulty of choosing an appropriate energy window, as no discrete γ-photons are emitted (*7,8*). In ^{90}Y-FAPI therapy, lesion dosimetry is required for dose-response investigations and can be part of the decision-making process regarding the application of further therapeutic cycles.

As an alternative to bremsstrahlung imaging, ^{90}Y PET can be performed (*9*) to provide higher visual image quality and higher detectability for small lesions (*6,8*). Moreover, the possibility of reliable ^{90}Y PET quantification for selective internal radiation therapy was demonstrated (*10*). However, tumor activity concentrations in selective internal radiation therapy are typically high (>1 MBq/mL) (*11*), whereas in systemic radionuclide therapies, considerably lower

activity concentrations are accumulated by the tumor tissue (*3*). As ^{90}Y PET imaging is limited by poor counting statistics due to internal positron–electron pair conversion occurring in only 0.00326% of pairs per decay (*11*), quantification of low activity concentrations is extremely challenging (*12*).

The recently introduced digital silicon photomultiplier-based PET/CT systems offer higher effective sensitivity and higher spatial and coincidence timing resolutions than previous-generation systems. Therefore, image quality and lesion detectability are improved, particularly for small lesions with low tracer uptake (*13–17*). The improvements were described for different radionuclides, including ^{18}F (positron branching ratio, 97%) and ^{68}Ga (positron branching ratio, 89%), and for the nonstandard tracer ^{124}I (23%). Recently, first applications of digital ^{90}Y PET in the context of selective internal radiation therapy were described (*12,18*) but—to our knowledge—no performance evaluation for systemic radionuclide therapy has been performed yet.

The aim of this study was to explore the conditions for reliable lesion image quantification in ^{90}Y-FAPI radionuclide therapy using a digital PET/CT system.

MATERIALS AND METHODS

Study Design

The study consisted of 2 parts: a phantom study and a clinical case study. A National Electrical Manufacturers Association (NEMA) tumor phantom and an anthropomorphic abdominal tumor phantom were scanned under different conditions to estimate the size-dependent minimum detectable activity concentration (MDAC), minimum quantifiable activity concentration (MQAC), and quantification accuracy. Two approaches for partial-volume effect correction were compared. Additionally, tumor dosimetry for 3 patients treated with ^{90}Y-FAPI was performed and evaluated, considering the results of the phantom data. A condensed version of the methods used is given in this article; full experimental details are presented as supplemental materials (supplemental materials are available at http://jnm.snmjournals.org).

Simple Approaches to Correct for Partial-Volume Effects

In clinical tumor dosimetry, the mean imaged activity concentration within the tumor boundary is commonly used to derive the (mean) tumor absorbed (radiation) dose. When the mean activity concentration is used, a partial-volume effect correction is necessary unless the objects are extremely large, that is, an equivalent sphere diameter of greater than or equal to 47 times the PET spatial resolution (*19*). Two simple approaches were applied in this study to correct for this effect. In the first, the contour-based approach, measured sphere recovery coefficient (RC) values were used to correct the mean imaged activity concentration within the lesion boundary. RC values were derived from the NEMA tumor phantom. The second approach, the oversized volume-of-interest (VOI)–based approach, included the total activity within the lesion volume using an oversized VOI, whose borders had an approximate distance of 1 time the PET spatial resolution of the actual geometric (CT-derived) boundary of the lesion. It was assumed that this oversized VOI contained the main activity to compensate for partial-volume effects; however, to compensate for a contribution from background activity, a background subtraction was performed as previously described (*20*).

Phantoms

Setup and Preparation. The NEMA tumor phantom is a torso-shaped phantom containing 6 spheres (with diameters of 9.7, 12.6, 17.4, 22.2, 27.7, and 37.0 mm). The anthropomorphic abdominal tumor phantom (Abdo-Man) (*21*) contains a refillable liver insert, in which 4 spheres (diameters of 10.0, 20.0, 30.0, and 40.0 mm) are attached. It was selected from the phantoms available at our institution

(University Hospital Essen) to resemble the human body scattering geometry more realistically than the NEMA tumor phantom. Moreover, an investigation of quantification accuracy with the NEMA phantom would have been biased for the contour-based method, as the RC values were determined using images of the same phantom.

On the basis of clinical data, spheric inserts and the cavity were filled with ^{90}Y solution at a representative initial sphere activity concentration of about 3.3 MBq/mL and a signal-to-background ratio of about 40. The initial activity concentration was determined as the mean of measurements using 3 different calibrated vial geometries in 2 different dose calibrators; the maximum error of the initial activity concentration was estimated to be $\pm7\%$ at the 95% confidence level (Supplemental Table 1). Activity concentrations at the PET start time were 3.36, 1.96, 1.22, 0.73, 0.34, 0.20, 0.12, and 0.05 MBq/mL for the NEMA tumor phantom and 3.33, 1.97, 1.23, 0.73, 0.34, 0.20, 0.12, and 0.06 MBq/mL for the anthropomorphic tumor phantom.

PET Acquisition and Image Reconstruction. Phantom PET data were acquired using a single bed position on a digital Biograph Vision 600 PET/CT scanner (Siemens Healthineers; detailed specifications are given in Supplemental Table 2), which exhibits a time-of-flight resolution of 210 ps (*22*). Initially, the NEMA tumor phantom was scanned for 6 h to determine RC values at high counting statistics. Thereafter, PET data for both phantoms were acquired for 30 min and used to reconstruct 30- and 15-min acquisition time PET images.

Images were reconstructed with the time-of-flight option and with point spread function modeling as previously recommended for quantitative ^{90}Y PET imaging on the Biograph Vision scanner (*12*). Two postreconstruction smoothing filter levels (all-pass and 5-mm gaussian filters) were applied. The images had a voxel size of $3.30 \times 3.30 \times 3.00$ mm, and the measured system spatial resolution (average full width at half maximum) (*23*) was 6.0 mm for a 5-mm gaussian smoothing filter.

Patients

Patient Characteristics. Retrospective analysis of clinical data was approved by the local ethics committee (permit no. 20-9558-BO). Datasets for 3 patients who had progressive, advanced-stage solitary fibrous tumor (SFT) and received ^{90}Y-FAPI-46 therapy (first cycle) under compassionate access after clinical indication were included. The decision about radionuclide treatment was made by a multidisciplinary tumor board. All patients had either previously shown progressive disease during established treatment options or were not eligible for other established treatment concepts. The administered therapeutic activities were 8.90 GBq (patient 1), 3.82 GBq (patient 2), and 3.67 GBq (patient 3).

PET Acquisition and Image Reconstruction. PET/CT examinations were scheduled as described in a previous study (*3*). Because of symptomatic patients and logistical reasons, serial PET/CT acquisitions were performed at slightly different time points: 17, 22, and 41 h after injection for patient 1; 2, 20, and 43 h after injection for patient 2; and 1, 4, and 20 h after injection for patient 3. PET data acquisition and image reconstruction were performed as described for phantoms (15-min acquisition time per bed position and 5-mm gaussian smoothing filter).

Phantom Analysis

MDAC. The images of the NEMA tumor phantom at various activity concentrations were used to determine the MDAC as previously described (*13,24*). In brief, the visual detectability of each sphere was determined in a human observer study. Next, the signal-to-noise ratio (SNR) of each sphere was determined to estimate the SNR threshold indicating detectability. Finally, the MDAC was calculated for each sphere. The MDAC was defined as the activity concentration at the threshold SNR.

Quantification Accuracy Evaluation. To evaluate the lesion quantification accuracy, the activity concentration ratio of PET-imaged measurements to (decay-corrected) dose calibrator–derived measurements

was investigated. A ±20% deviation range of the activity concentration ratio was regarded as acceptable considering the uncertainty for the ^{90}Y activity concentration dose calibrator measurement, the ^{18}F PET cross-calibration measurement (25), and the frequency of the positron–electron pair conversion (26–29).

MQAC. The results of the quantification accuracy evaluations were used to estimate the MQAC, that is, the minimum activity concentration for which the quantification appears to be reliable. In its derivation, the values for the quantification accuracy should lie within the ±20% deviation range.

Patient Analysis

In the patient analysis, key quantities related to the estimation of the tumor absorbed dose were derived. The procedure used was previously described (3). In brief, the tumor volumes were estimated by manual segmentation (VOI technique) using the respective CT images, and the VOIs were used to determine the tumor uptake values at 3 imaging time points. Mean tumor activity concentrations were determined using both the contour-based approach and the oversized VOI–based approach. The resulting uptake curves were parameterized by fitting a monoexponential function to the measured uptake values to determine the effective half-lives. The time-integrated activity coefficients (residence times) were determined and used to estimate the tumor absorbed doses with the sphere model of OLINDA/EXM (30). A logarithmic approach was applied for interpolation between tumor absorbed doses in the OLINDA tables.

Software/Statistics

PET image analysis and VOI segmentation were performed using PMOD 4.202 (PMOD Technologies); MATLAB R2021a (The MathWorks) was used for data handling and computations. The tumor absorbed dose was calculated using OLINDA/EXM 2.2 software (Hermes Medical Solutions AB). Graphics were created using BioRender.com (BioRender; www.BioRender.com).

RESULTS

Recovery Coefficients

Fitting parameters for calculating measured and fitted RC values are listed in Supplemental Table 3. The agreement between fitted and measured RC values was high (maximum percentage deviation of –6%), indicating a small contribution of the fitting process to the total error of the quantification approaches.

MDAC

Figure 1 shows exemplary PET images for the NEMA tumor phantom. The human observer study revealed an SNR threshold of greater than or equal to 6 for distinguishing between spheres that were not detected and spheres that were detected (Supplemental Fig. 1). The MDAC for each sphere size is shown in Table 1. The SNR is presented as a function of the activity concentration for all acquisition conditions in Supplemental Figure 2. The 5-mm smoothed images provided improved detectability for smaller spheres, and the MDAC was smaller by a mean factor of 0.54 in comparison with the results for images without gaussian smoothing. For a 30-min acquisition time, the MDAC was reduced by a factor of 0.53 compared with that for a 15-min acquisition time.

As the detectability was higher for the 5-mm gaussian filter, the following evaluation of the anthropomorphic phantom and patient examples was restricted to this filter level. Moreover, an acquisition time of 30 min per bed position is excessively long and not feasible for patients who are in pain and undergoing ^{90}Y-FAPI-46 therapy (typically, a PET scan comprises at least 2 bed positions); therefore, only an acquisition time of 15 min (per bed position) was further evaluated.

Figure 2 shows exemplary PET maximum-intensity projections (MIPs) of the anthropomorphic abdominal tumor phantom. Only detectable spheres were included in the quantification accuracy analysis (detectable was defined as an activity concentration greater than or equal to the size-dependent MDAC; the MDAC for the 9.7-, 17.4-, 27.7-, and 37.0-mm spheres in the NEMA tumor phantom were used for the 10.0-, 20.0-, 30.0-, and 40.0-mm spheres in the anthropomorphic abdominal tumor phantom).

Quantification accuracy results from the contour-based and oversized VOI–based quantification approaches are shown in Figure 3. For the 40- and 30-mm spheres, accurate quantification was feasible for detectable lesions using both approaches. The oversized VOI–based approach revealed slightly more accurate results for the 30-mm sphere. For the 20-mm sphere and activity concentrations of less than or equal to 1.23 MBq/mL, quantification accuracy for the contour-based method was slightly below the –20% deviation threshold, whereas accurate quantification was feasible down to activity concentrations of greater than or equal to 0.34 MBq/mL using the
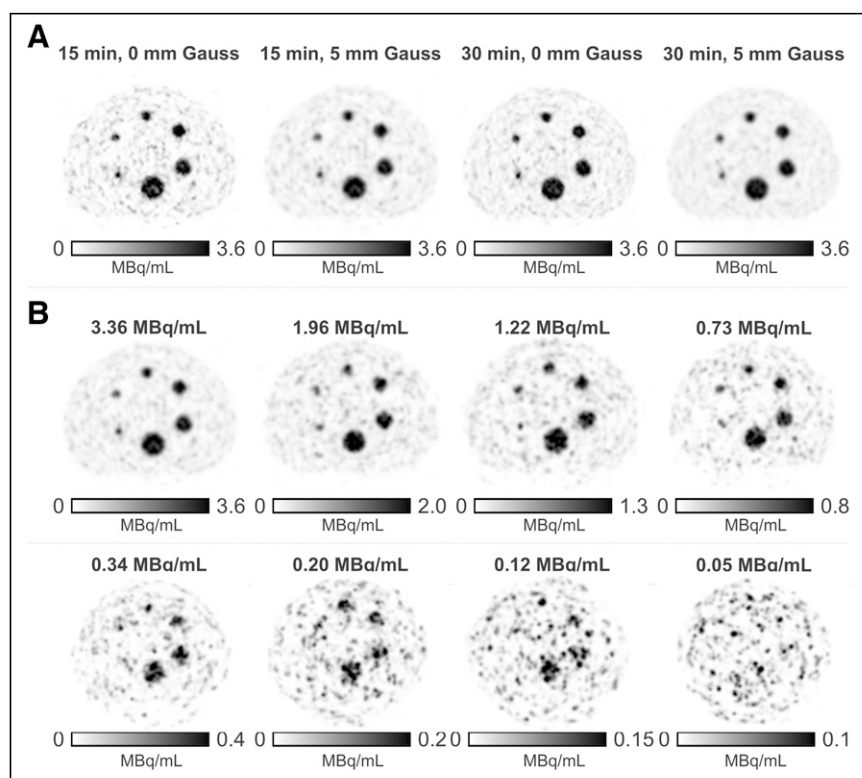
FIGURE 1. PET images of NEMA tumor phantom showing different investigated emission times and gaussian filter levels at highest sphere activity concentration of 3.36 MBq/mL (A) and different investigated sphere activity concentrations for 15-min acquisition time and 5-mm gaussian smoothing level (B).

TABLE 1
Estimated MDAC for Investigated Sphere Diameters, Acquisition Time Durations, and Smoothing Levels

Sphere diameter (mm)	Estimated MDAC (MBq/mL)			
	All-pass filter		5-mm gaussian smoothing filter	
	15 min	30 min	15 min	30 min
9.7	0.71	0.44	0.43	0.33
12.6	0.51	0.23	0.30	0.17
17.4	0.37	0.15	0.16	0.07
22.2	0.37	0.18	0.18	0.09
27.7	0.29	0.16	0.15	0.08
37.0	0.27	0.14	0.12	0.06

oversized VOI–based approach. For the smallest (10-mm-diameter) sphere, quantification accuracy was limited for activity concentrations of less than or equal to 1.23 MBq/mL, and the contour-based approach revealed slightly more accurate results. In general, a trend toward an underestimation of the activity concentration was observed for low activity concentrations.

MQAC

The MQAC ranged from 0.12 MBq/mL for the 40-mm sphere to 1.97 MBq/mL for the 10-mm sphere. Detailed results are presented in Table 2.

Patient Tumor Dosimetry

Lesion dosimetry was performed for 3 tumor sites in 3 patients with thoracic/pleural SFT. In patient 1, a left paracardial supradiaphragmatic SFT was evaluated; in patient 2, a right lateral SFT of the third thoracic vertebra was evaluated; and in patient 3, a left lateral SFT of the aortic arch was evaluated (Figs. 4–6). Almost all activity concentration measurements were considered reliable
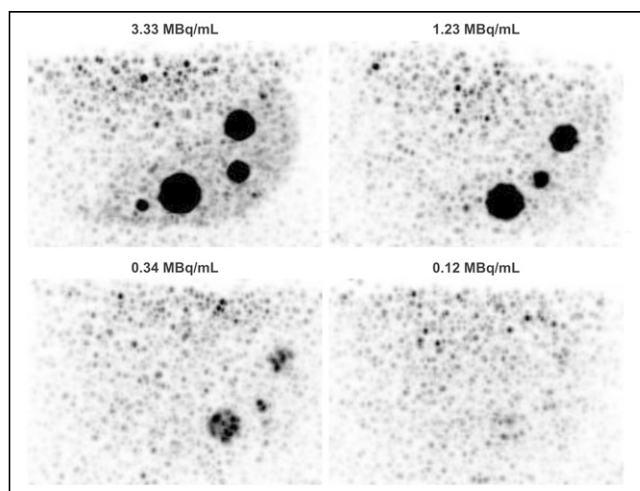
FIGURE 2. PET MIP images of anthropomorphic abdominal tumor phantom at 4 different activity concentration levels. Images were reconstructed using 15-min acquisition data and smoothed with 5-mm gaussian filter. In the MIP images, the largest sphere is marginally discernible at 0.12 MBq/mL.
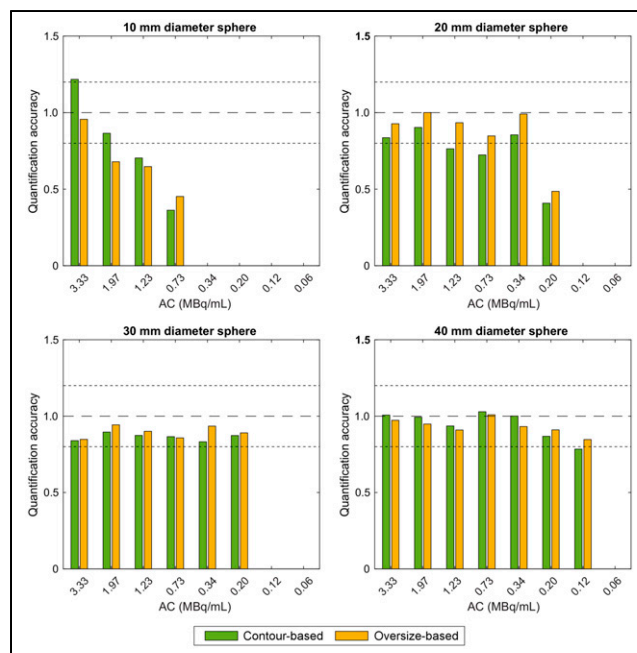
FIGURE 3. Contour-based and oversized VOI–based quantification accuracy using anthropomorphic tumor phantom. Dashed horizontal lines indicate ±20% error margins. Missing bars correspond to spheres regarded as "not detected" and as such not considered for quantification accuracy evaluation. Only PET images with 5-mm gaussian filter and acquisition time of 15 min (per bed position) were analyzed. AC = activity concentration.

(Fig. 7). The activity concentration at the last measurement in patient 1 was below the MQAC for the largest sphere investigated in the phantom study (sphere diameter of 40 mm), which is why we did not use the data point for the lesion dosimetry estimation.

The relevant key dosimetry data derived from both the oversized VOI–based and the contour-based quantification approaches are listed in Table 3. The tumor absorbed dose estimation ranged from 0.6 to 12.0 Gy/GBq. Overall good agreement (absolute percentage deviation of <20%) of the relevant quantities was observed between the 2 approaches, except for the effective half-life of the tumor in patient 1 (8.4 vs. 12.2 h).

DISCUSSION

FAP-targeted radionuclide therapy is emerging for patients with solid tumors and, recently, several case reports and case series using different ligands and radionuclides were published (31–33). For example, ^{90}Y-FAPI therapy was described for the treatment of sarcoma and pancreatic cancer patients (3,4) as well as a patient

TABLE 2
Estimated MQAC of Reliability at Lesion Sizes Derived From Images Reconstructed with 15-min Acquisition Time Data and Smoothed with 5-mm Gaussian Filter

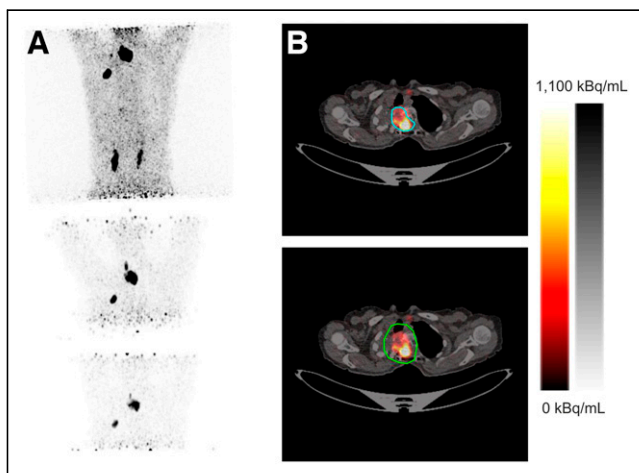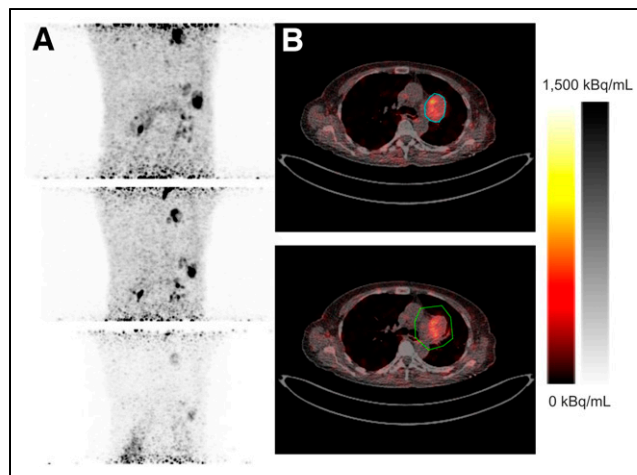| Lesion diameter (mm)	MQAC (MBq/mL)
10	1.97
20	0.34
30	0.20
40	0.12
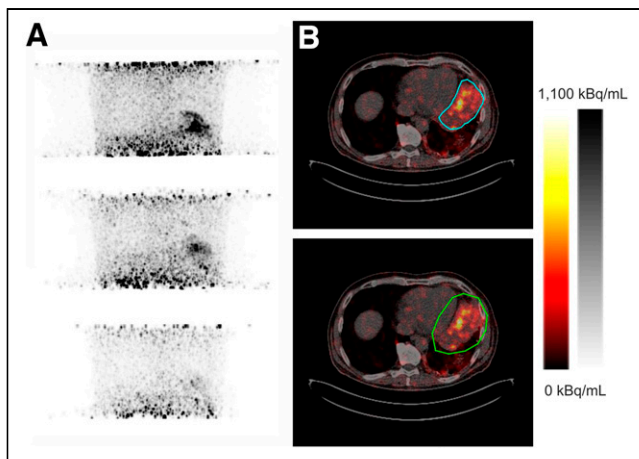
FIGURE 4. PET/CT imaging and lesion delineation for patient 1. ^{90}Y-FAPI-46 PET MIP images (A) and axial PET/CT images (B) show contour-based VOI (blue) and oversized VOI (green). Only first 2 PET data points were considered for tumor absorbed dose estimation.

FIGURE 6. PET/CT imaging and lesion delineation for patient 3. ^{90}Y-FAPI-46 PET MIP images (A) and axial PET/CT images (B) show contour-based VOI (blue) and oversized VOI (green).

with both breast and colorectal cancers (*34*). Safety and efficacy studies, including dosimetry, have been reported for ^{177}Lu-labeled FAP–targeted radionuclide therapy (*32,35*). Given that ^{90}Y-based dosimetry for systemic radioligand therapy is not as well established and documented as ^{177}Lu-based dosimetry, it is even more important to establish the basis for accurate radionuclide quantification. Doing so will have relevance in pharmacovigilance processes of authorization (such as the evaluation of safety) in the form of dosimetry for organs at risk and efficacy in the form of tumor dosimetry for investigating the dose effects of novel ^{90}Y radioligand therapy agents.

In the present study, we applied a heuristic approach for reliable lesion quantification in ^{90}Y-FAPI therapy. To the best of our knowledge, no reports on reliable PET-derived ^{90}Y tumor quantification for activity concentration ranges as they appear in systemic radionuclide therapies have yet been published. The phantom evaluation (Figs. 1 and 2) showed that for detectable lesions greater than or equal to 30 mm in diameter, reliable quantification is feasible (Fig. 3). For the 20-mm-diameter sphere, the difference between the MQAC and the MDAC was small (0.34 vs. 0.16 MBq/mL).

FIGURE 5. PET/CT imaging and lesion delineation for patient 2. ^{90}Y-FAPI-46 PET MIP images (A) and axial PET/CT images (B) show contour-based VOI (blue) and oversized VOI (green).

Only for the smallest sphere (10-mm diameter) was the MQAC notably higher than the MDAC (1.97 vs. 0.43 MBq/mL). Possible explanations are the low absolute amount of ^{90}Y activity resulting in poor counting statistics and the proximity to the 40-mm sphere (also, see a comparison of MDACs between NEMA and anthropomorphic phantoms in the supplemental materials and Supplemental Table 4).

In current clinical scenarios, patients undergoing ^{90}Y-FAPI-46 therapy will most likely exhibit larger tumor masses, as this therapy is offered in end-stage diseases when established therapy options have already been exhausted (*3,4*). In the evaluated patients (Figs. 4–7), the accumulated tumor activity concentration was, except for 1 data point, larger than the size-dependent MQAC of 0.12 MBq/mL (40-mm-diameter lesion). We therefore assume that reliable quantification in the context of intratherapeutic tumor dosimetry is feasible in ^{90}Y-FAPI-46 therapy using a digital PET/CT system. The tumor absorbed dose estimation ranged from 0.6 to 12.0 Gy/GBq (Table 3).

As cancer-associated fibroblasts were described to be nonuniformly distributed in the tumor microenvironment (*36*), ^{90}Y-FAPI accumulation will most likely follow that pattern and lead to nonuniform tumor uptake in PET imaging. Because the high β-particle energy of ^{90}Y leads to a high particle range, tumor cells surrounding FAP-expressing cancer-associated fibroblasts will be targets of crossfire and bystander radiation (*37*). Therefore, ^{90}Y—which deposits its energy at a distance of up to 1 cm—may be more suitable for FAPI radionuclide therapy than ^{177}Lu—with an energy deposition in close proximity to the source (*38*). However, the consequences of nonuniform FAPI uptake for the quantification of accumulated activity, dosimetry, and the dose response remain unclear. In the present study, quantification approaches were projected without adjustments from the homogeneous conditions of the phantom study to the patient images. Therefore, accumulated activity was measured as the mean activity concentration. This approach might be appropriate given a high level of influence of crossfire and bystander effects, which might lead to a homogenization of the radiation dose. Voxel-based dosimetry might be an alternative to take into account a nonuniform activity distribution (*39*); however, its clinical relevance might be limited by the low accumulated activity concentrations in systemic ^{90}Y radionuclide therapy.

Future evaluations of clinical data will be necessary to investigate possible effects on determined tumor doses and, especially,
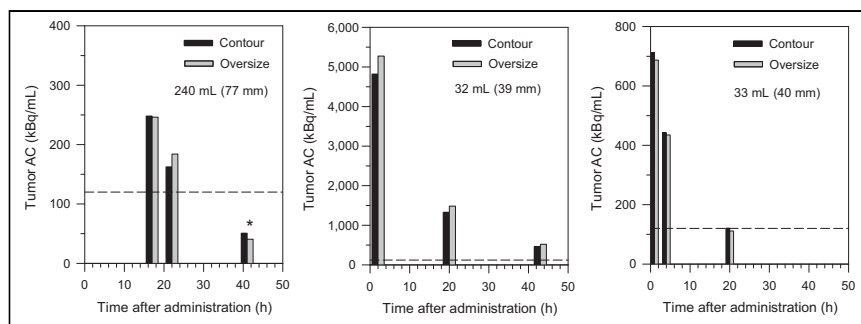
FIGURE 7. Tumor activity concentration (AC) derived from either contour-based or oversized VOI–based approach as function of time after administration (3 time points). Values within parentheses are respective equivalent sphere diameters. ACs above horizontal dashed lines indicate reliable quantification based on Figure 3. Asterisk indicates value that appears to be "unreliable" in terms of quantification (see text for details).

dose-response effects to select the optimal quantification approach. With increasing application of ^{90}Y FAPI therapy, sufficient data will probably be available for a systematic evaluation. At the moment, the number of investigated patients with sufficient follow-up data is limited. In the present study, we investigated the quantification accuracy of a current-generation PET scanner as a basis for future clinical evaluations.

The comparison of 15- and 30-min acquisition times per bed position revealed a lower MDAC for the 30-min acquisition time, by a factor of approximately 2 (Table 1). Thus, an approximate linear correlation between MDAC and acquisition time was observed. This finding is in line with the results of a previous study using a different radionuclide (13). Typically, PET scans in patients receiving ^{90}Y-based therapy are performed using at least 2 bed positions (3). Therefore, in most patients, an extension of the acquisition time will most likely not be tolerable. Moreover, detectability was improved when a 5-mm gaussian filter was applied (Table 1). In a systematic comparison of previous-generation Siemens PET/CT systems for quantitative ^{90}Y imaging, the use of a gaussian filter was left to the user's decision (40). We therefore propose an acquisition time of 15 min for clinical imaging protocols and the application of a 5-mm gaussian filter.

Both evaluated quantification methods exhibit limitations and advantages. On the one hand, the contour-based approach is more reproducible, but it has no background activity concentration correction. On the other hand, although the oversized VOI–based approach will represent the lesion activity surrounded by a uniform and low activity concentration background, accounting for a nonuniform background might be challenging, making the quantification prone to error. Regarding quantification accuracy in phantom data and estimated activity concentrations in patient data, both methods yielded comparable results (Figs. 3 and 7), probably because of a low and visually uniform background. Larger differences might be possible for tumor lesions close to a region with high physiologic tracer accumulation, such as the kidney.

Only a few previous studies investigating ^{90}Y PET imaging in the context of systemic radionuclide therapy were published, and none of these used a digital PET system. Fabbri et al. (41) identified an MDAC of 0.20 MBq/mL for the 3 largest spheres of the NEMA tumor phantom using a previous-generation time-of-flight–capable PET scanner. In that study, 30-min acquisitions with no background activity were reconstructed with 3-dimensional ordered-subset expectation maximization using 2 iterations and 4 subsets and a 5-mm gaussian filter. In the present study, for a 30-min acquisition time, the MDAC was smaller (0.06–0.09 MBq/mL) (Table 1). The improvement is explained by the improved time-of-flight resolution of the digital PET system and is comparable to the improvement that we observed in a direct comparison of 2 PET/CT systems for ^{124}I (13). Of note, Fabbri et al. (41) did not investigate quantification accuracy. Walrand et al. (42) also investigated previous-generation PET systems (42); they predicted a reliable estimation of the mean absorbed kidney dose after ^{90}Y-DOTATOC therapy using a kidney phantom filled with an activity concentration of about 0.33 MBq/mL—substantially larger than the MQAC for the largest sphere in the present study (0.12 MBq/mL). Moreover, the investigated kidney cortex had a volume of 107 mL—considerably larger than the largest sphere in the present study (sphere volume of 33.5 mL).

Future improvements might be possible through the application of total-body PET/CT scanners (43), which cover an extended field of view and allow complete acquisition of all necessary PET data in a patient scan using a single bed position. Moreover, increased sensitivity may allow for shorter acquisition times (44) or, alternatively, improved accuracy of detection and quantification of lesions at lower activity concentrations.

TABLE 3
Key Dosimetry Quantities for Estimating Tumor AD per Administered Activity Using Contour-Based and Oversized VOI–Based Approaches

Patient	V (mL)	d (mm)	Contour-based			Oversized VOI-based		
			TIAC (min)	T_{eff} (h)	AD (Gy/GBq)	TIAC (min)	T_{eff} (h)	AD (Gy/GBq)
1	240	77	17	8.4	0.62	17	12.2	0.60
2	32	39	42	12.3	10.90	47	12.4	12.00
3	33	40	4	7.5	0.98	4	7.3	0.93

AD = absorbed dose; VOI = volume of interest; V = tumor volume; d = equivalent sphere diameter; TIAC = time-integrated activity coefficient; T_{eff} = effective half-life.

CONCLUSION

For ^{90}Y-treated lesions with a diameter of greater than or equal to 40 mm—typical in patients receiving FAPI radionuclide therapy—reliable quantification was possible for activity concentrations of at least 0.12 MBq/mL using a digital PET system. For lesions with a diameter of greater than or equal to 30 mm, the minimum detectable activity and minimum quantifiable activity were in good agreement, suggesting that dosimetry can be performed for detectable lesions. Further dosimetry studies are needed to thoroughly investigate the efficacy and safety of novel ^{90}Y-FAPI radionuclide therapies.

DISCLOSURE

ACKNOWLEDGMENT

KEY POINTS

QUESTION: Does digital PET allow reliable quantification for lesion dosimetry in ^{90}Y-FAPI radionuclide therapy?

PERTINENT FINDINGS: For lesion sizes and activity concentrations that are expected to be observed in patients treated with ^{90}Y-FAPI, quantification with reasonable accuracy is possible.

IMPLICATIONS FOR PATIENT CARE: Reliable lesion dosimetry in ^{90}Y-FAPI radionuclide therapy is mandatory for dose-response evaluations and for decisions about treatment continuation.

REFERENCES

1. Dancey JE, Shepherd FA, Paul K, et al. Treatment of nonresectable hepatocellular carcinoma with intrahepatic ^{90}Y-microspheres. *J Nucl Med.* 2000;41:1673–1681.
2. Strosberg J, El-Haddad G, Wolin E, et al. Phase 3 trial of ^{177}Lu-Dotatate for midgut neuroendocrine tumors. *N Engl J Med.* 2017;376:125–135.
3. Ferdinandus J, Costa PF, Kessler L, et al. Initial clinical experience with ^{90}Y-FAPI-46 radioligand therapy for advanced-stage solid tumors: a case series of 9 patients. *J Nucl Med.* 2022;63:727–734.
4. Fendler WP, Pabst KM, Kessler L, et al. Safety and efficacy of ^{90}Y-FAPI-46 radioligand therapy in patients with advanced sarcoma and other cancer entities. *Clin Cancer Res.* 2022; Epub ahead of print.
5. Liu F, Qi L, Liu B, et al. Fibroblast activation protein overexpression and clinical implications in solid tumors: a meta-analysis. *PLoS One.* 2015;10:e0116683.
6. Brosch J, Gosewisch A, Kaiser L, et al. 3D image-based dosimetry for yttrium-90 radioembolization of hepatocellular carcinoma: impact of imaging method on absorbed dose estimates. *Phys Med.* 2020;80:317–326.
7. Elschot M, Vermolen BJ, Lam MG, de Keizer B, van den Bosch MA, de Jong HW. Quantitative comparison of PET and Bremsstrahlung SPECT for imaging the in vivo yttrium-90 microsphere distribution after liver radioembolization. *PLoS One.* 2013;8:e55742.
8. Kubik A, Budzynska A, Kacperski K, et al. Evaluation of qualitative and quantitative data of Y-90 imaging in SPECT/CT and PET/CT phantom studies. *PLoS One.* 2021;16:e0246848.
9. Wright CL, Zhang J, Tweedle MF, Knopp MV, Hall NC. Theranostic Imaging of yttrium-90. *BioMed Res Int.* 2015;2015:481279.
10. Lhommel R, van Elmbt L, Goffette P, et al. Feasibility of ^{90}Y TOF PET-based dosimetry in liver metastasis therapy using SIR-Spheres. *Eur J Nucl Med Mol Imaging.* 2010;37:1654–1662.
11. Pasciak AS, Bourgeois AC, McKinney JM, et al. Radioembolization and the dynamic role of ^{90}Y PET/CT. *Front Oncol.* 2014;4:38.
12. Kunnen B, Beijst C, Lam M, Viergever MA, de Jong H. Comparison of the Biograph Vision and Biograph mCT for quantitative ^{90}Y PET/CT imaging for radioembolisation. *EJNMMI Phys.* 2020;7:14.
13. Kersting D, Jentzen W, Fragoso Costa P, et al. Silicon-photomultiplier-based PET/CT reduces the minimum detectable activity of iodine-124. *Sci Rep.* 2021;11:17477.
14. Weber M, Jentzen W, Hofferber R, et al. Evaluation of [^{68}Ga]Ga-PSMA PET/CT images acquired with a reduced scan time duration in prostate cancer patients using the digital Biograph Vision. *EJNMMI Res.* 2021;11:21.
15. Weber M, Jentzen W, Hofferber R, et al. Evaluation of ^{18}F-FDG PET/CT images acquired with a reduced scan time duration in lymphoma patients using the digital Biograph Vision. *BMC Cancer.* 2021;21:62.
16. Fragoso Costa P, Jentzen W, Sußelbeck F, et al. Reduction of emission time for [^{68}Ga]Ga-PSMA PET/CT using the digital Biograph Vision: a phantom study. *Q J Nucl Med Mol Imaging.* July 26, 2021 [Epub ahead of print].
17. Kersting D, Jentzen W, Sraieb M, et al. Comparing lesion detection efficacy and image quality across different PET system generations to optimize the iodine-124 PET protocol for recurrent thyroid cancer. *EJNMMI Phys.* 2021;8:14.
18. Labour J, Boissard P, Baudier T, et al. Yttrium-90 quantitative phantom study using digital photon counting PET. *EJNMMI Phys.* 2021;8:56.
19. Jentzen W. Experimental investigation of factors affecting the absolute recovery coefficients in iodine-124 PET lesion imaging. *Phys Med Biol.* 2010;55:2365–2398.
20. Walrand S, Jamar F, Mathieu I, et al. Quantitation in PET using isotopes emitting prompt single gammas: application to yttrium-86. *Eur J Nucl Med Mol Imaging.* 2003;30:354–361.
21. Gear JI, Cummings C, Craig AJ, et al. Abdo-Man: a 3D-printed anthropomorphic phantom for validating quantitative SIRT. *EJNMMI Phys.* 2016;3:17.
22. van Sluis J, de Jong J, Schaar J, et al. Performance characteristics of the digital Biograph Vision PET/CT system. *J Nucl Med.* 2019;60:1031–1036.
23. Jentzen W, Weise R, Kupferschlager J, et al. Iodine-124 PET dosimetry in differentiated thyroid cancer: recovery coefficient in 2D and 3D modes for PET(/CT) systems. *Eur J Nucl Med Mol Imaging.* 2008;35:611–623.
24. Øen SK, Aasheim LB, Eikenes L, Karlberg AM. Image quality and detectability in Siemens Biograph PET/MRI and PET/CT systems: a phantom study. *EJNMMI Phys.* 2019;6:16.
25. Keller SH, Jakoby B, Svalling S, Kjaer A, Hojgaard L, Klausen TL. Cross-calibration of the Siemens mMR: easily acquired accurate PET phantom measurements, long-term stability and reproducibility. *EJNMMI Phys.* 2016;3:11.
26. Dryák P, Solc J. Measurement of the branching ratio related to the internal pair production of Y-90. *Appl Radiat Isot.* 2020;156:108942.
27. Chistsé V, Bé MM. [90]Y: comments on evaluation of decay data. Decay Data Evaluation Project website. http://www.nucleide.org/DDEP_WG/Nuclides/Y-90_com.pdf. Updated November 2016. Accessed March 3, 2022.

28. Staníček J. Emission of positrons in beta-decay of ^{90}Sr $+$ ^{90}Y. *Acta Phys Univ Comen.* 2007;XLVIII–XLIX:51–56.

29. Selwyn RG, Nickles RJ, Thomadsen BR, DeWerd LA, Micka JA. A new internal pair production branching ratio of ^{90}Y: the development of a non-destructive assay for ^{90}Y and ^{90}Sr. *Appl Radiat Isot.* 2007;65:318–327.

30. Stabin MG, Sparks RB, Crowe E. OLINDA/EXM: the second-generation personal computer software for internal dose assessment in nuclear medicine. *J Nucl Med.* 2005;46:1023–1027.

31. Assadi M, Rekabpour SJ, Jafari E, et al. Feasibility and therapeutic potential of ^{177}Lu-fibroblast activation protein inhibitor-46 for patients with relapsed or refractory cancers: a preliminary study. *Clin Nucl Med.* 2021;46:e523–e530.

32. Ballal S, Yadav MP, Moon ES, et al. First-in-human results on the biodistribution, pharmacokinetics, and dosimetry of [^{177}Lu]Lu-DOTA.SA.FAPi and [^{177}Lu]Lu-DOTAGA.(SA.FAPi)$_2$. *Pharmaceuticals (Basel).* 2021;14:1212.

33. Fu K, Pang Y, Zhao L, et al. FAP-targeted radionuclide therapy with [^{177}Lu]Lu-FAPI-46 in metastatic nasopharyngeal carcinoma. *Eur J Nucl Med Mol Imaging.* 2022;49:1767–1769.

34. Rathke H, Fuxius S, Giesel FL, et al. Two tumors, one target: preliminary experience with ^{90}Y-FAPI therapy in a patient with metastasized breast and colorectal cancer. *Clin Nucl Med.* 2021;46:842–844.

35. Kuyumcu S, Kovan B, Sanli Y, et al. Safety of fibroblast activation protein-targeted radionuclide therapy by a low-dose dosimetric approach using ^{177}Lu-FAPI04. *Clin Nucl Med.* 2021;46:641–646.

36. Sahai E, Astsaturov I, Cukierman E, et al. A framework for advancing our understanding of cancer-associated fibroblasts. *Nat Rev Cancer.* 2020;20:174–186.

37. Freudenberg R, Wendisch M, Kotzerke J. Geant4-Simulations for cellular dosimetry in nuclear medicine. *Z Med Phys.* 2011;21:281–289.

38. Brady D, O'Sullivan JM, Prise KM. What is the role of the bystander response in radionuclide therapies? *Front Oncol.* 2013;3:215.

39. Chiesa C, Bardies M, Zaidi H. Voxel-based dosimetry is superior to mean absorbed dose approach for establishing dose-effect relationship in targeted radionuclide therapy. *Med Phys.* 2019;46:5403–5406.

40. Willowson KP, Tapner M, Team QI, Bailey DL. A multicentre comparison of quantitative ^{90}Y PET/CT for dosimetric purposes after radioembolization with resin microspheres: the QUEST Phantom Study. *Eur J Nucl Med Mol Imaging.* 2015;42:1202–1222.

41. Fabbri C, Bartolomei M, Mattone V, et al. ^{90}Y-PET/CT imaging quantification for dosimetry in peptide receptor radionuclide therapy: analysis and corrections of the impairing factors. *Cancer Biother Radiopharm.* 2015;30:200–210.

42. Walrand S, Jamar F, van Elmbt L, Lhommel R, Bekonde EB, Pauwels S. 4-Step renal dosimetry dependent on cortex geometry applied to ^{90}Y peptide receptor radiotherapy: evaluation using a fillable kidney phantom imaged by ^{90}Y PET. *J Nucl Med.* 2010;51:1969–1973.

43. Zhang YQ, Hu PC, Wu RZ, et al. The image quality, lesion detectability, and acquisition time of ^{18}F-FDG total-body PET/CT in oncological patients. *Eur J Nucl Med Mol Imaging.* 2020;47:2507–2515.

44. Alberts I, Hunermund JN, Prenosil G, et al. Clinical performance of long axial field of view PET/CT: a head-to-head intra-individual comparison of the Biograph Vision Quadra with the Biograph Vision PET/CT. *Eur J Nucl Med Mol Imaging.* 2021;48:2395–2404.